International Journal of Nanomedicine

Dovepress
Taylor & Francis Group

Open Access Full Text Article

ORIGINAL RESEARCH

Tumor Microenvironment Reprogramming via Copper-Enriched Black Phosphorus Nanoplatform for Cuproptosis-Sensitized Low-Dose Radioimmunotherapy

Yutong Chen[1,*], Jin Wang[2,*], Daniel Zheng[1,3], Weiyu Zhang[3]

[1]Department of Oncology, Shengli Clinical Medical College of Fujian Medical University, Fuzhou University Affiliated Provincial Hospital, Fuzhou, Fujian, 350001, People's Republic of China; [2]Department of Prenatal Diagnosis Center, Jinan Maternity and Child Care Hospital Affiliated to Shandong First Medical University, Jinan, 250001, People's Republic of China; [3]Center for Vascular Surgery and Interventional Oncology, Fuzhou University Affiliated Provincial Hospital, Fuzhou, 350001, People's Republic of China

*These authors contributed equally to this work

Correspondence: Weiyu Zhang, Fuzhou University Affiliated Provincial Hospital, Fuzhou, 350001, People's Republic of China, Email zhangwy55@alumni.sysu.edu.cn

Objective: Radioimmunotherapy (RIT) is a promising treatment for deep-seated and metastatic tumors, but its efficacy is limited by the immunosuppressive tumor microenvironment (TME) and a narrow therapeutic window. This study aimed to develop a novel nanoplatform to overcome these constraints by simultaneously sensitizing tumors to radiation, inducing cuproptosis, and reprogramming the immunosuppressive TME.

Methods: We engineered a PEGylated copper-loaded black phosphorus nanoplatform (BPNS@Cu-PEG). Its functionality as a radiosensitizer and cuproptosis inducer was evaluated. The mechanisms of TME reprogramming were investigated, including glutathione (GSH) depletion, reactive oxygen species (ROS) amplification, hypoxia alleviation, and M2-to-M1 macrophage repolarization. Furthermore, we systematically evaluated its antitumor immune effects in vitro and in vivo.

Results: BPNS@Cu-PEG was synthesized with a high copper incorporation rate of 93%. In vitro cellular assays confirmed that the internalized nanoplatform effectively induced cuproptosis and immunogenic cell death (ICD) while simultaneously regulating the TME. In vivo, BPNS@Cu-PEG not only potently inhibited tumor progression and stimulated robust antitumor immunity under low-dose radiotherapy but also exhibited an excellent safety profile.

Conclusion: This work establishes a copper-based, low-dose radioimmunotherapy strategy. The BPNS@Cu-PEG nanoplatform presents a viable and potent strategy to counteract radioresistance and promote systemic antitumor immunity, potentially broadening the therapeutic application and safety profile of RIT.

Keywords: radioimmunotherapy, immunogenic cell death, cuproptosis, tumor microenvironment, black phosphorus

Introduction

Radioimmunotherapy (RIT), which integrates radiotherapy with immunotherapy, has demonstrated considerable potential in suppressing tumor progression and metastasis.[1,2] Nevertheless, its clinical application is hampered by several inherent limitations. Radiotherapy is limited by normal tissue dose tolerance, and immunotherapy is challenged by interpatient heterogeneity and potential off-target toxicities.[1,3] Recently, immunogenic cell death (ICD) has emerged as a powerful strategy for broad-spectrum antitumor immunity.[4] Radiation-induced ICD facilitates the release of damage-associated molecular patterns (DAMPs), including calreticulin (CRT), high mobility group box 1 (HMGB1), and adenosine triphosphate (ATP), promoting dendritic cells (DCs) maturation and subsequent antitumor immune responses.[2,4,5]

Received: 16 September 2025
Accepted: 28 November 2025
Published: 5 December 2025

Despite this promise, clinical translation remains constrained by the immunosuppressive tumor microenvironment (TME) and the critical need to balance effective radiation doses with robust immune activation.[2,6]

In recent years, metal-based drugs have emerged as pivotal agents in tumor radiotherapy, offering unique mechanisms to overcome the limitations of conventional radiation therapy.[7,8] Their roles can be broadly categorized into two synergistic strategies. The first strategy leverages the high atomic number (Z) of certain metal ions, such as Gd,[9] Dy,[10] Au,[11,12] and Hf,[13,14] to enhance radiation energy absorption within tumors. When exposed to X-rays, these metal ions exhibit strong photoelectric and compton effects, significantly increasing localized energy deposition.[15–17] This phenomenon reduces the required radiation dose while maintaining therapeutic efficacy, thereby minimizing collateral damage to healthy tissues. The second strategy aims to reprogram the TME to enhance radiosensitivity. The TME is typically marked by elevated hydrogen peroxide (H_2O_2) and glutathione (GSH), as well as hypoxia, all of which contribute to radiation resistance.[18,19] Notably, Huang et al recently demonstrated the use of manganese (Mn) alone to modulate the TME and achieve effective low-dose radiotherapy.[20] The strategy of combining TME reprogramming with enhanced radiosensitivity provides a promising approach for low-dose tumor radioimmunotherapy, but it has not yet been fully explored.

Cuproptosis, a recently identified cell death pathway based on copper, offers a novel approach for cancer therapy.[21] This process involves copper ions binding to mitochondrial dihydrolipoamide S-acetyltransferase (DLAT), leading to DLAT oligomerization, proteotoxic stress, and mitochondrial dysfunction, ultimately resulting in tumor cell death.[21,22] As a unique mechanism of programmed cell death, cuproptosis shows considerable potential to overcome limitations of existing cancer therapies. Notably, emerging evidence indicates that cuproptosis can stimulate immune activation and enhance anti-tumor immunity through the release of DAMPs.[23–25] However, several challenges impede the effective induction of cuproptosis and its associated ICD. The sensitivity of tumor cuproptosis is also limited by the TME,[26] and the insufficient copper accumulation in tumors.[27] Moreover, the immunosuppressive TME, characterized by high infiltration of M2-type tumor-associated macrophages (TAMs), further suppresses ICD-mediated immune activation.[13,28] To harness the full immunotherapeutic potential of cuproptosis, it is essential to develop strategies that enhance copper delivery and counteract TME-mediated immunosuppression. Recent studies suggest that oxygen (O_2) can promote the repolarization of M2 macrophages toward the pro-inflammatory M1 phenotype.[26,29] Therefore, reprogramming the immunosuppressive TME offers a promising avenue to augment cuproptosis sensitivity and potentiate anti-tumor immunity.

Black phosphorus nanosheets (BPNS) are well-known two-dimensional nanomaterials with significant potential in achieving high-dose drug loading due to their high biocompatibility and large surface area.[30–32] Interestingly, BPNS function effectively as radiosensitizers; their high electron density and layered structure enable efficient interaction with ionizing radiation, thereby enhancing tumor cell sensitivity to radiotherapy.[33,34] Incorporating cuproptosis to enable low-dose radioimmunotherapy offers a potent yet underexplored approach for tumor treatment.

In this work, we developed a high-loading copper ion (Cu^{2+}) nanoplatform based on BPNS (denoted as BPNS@Cu) via metal-phosphorus coordination. Following PEGylation, the resulting BPNS@Cu-PEG nanocomplex exhibits enhanced X-ray deposition capability, enabling a reduction in the required radiation dose. The copper active center initiates a cascade of reactions that remodel the TME through GSH depletion, O_2 generation, and conversion to highly toxic hydroxyl radicals (•OH) formed by H_2O_2, collectively elevating oxidative stress and diminishing radioresistance. The resultant O_2 alleviates tumor hypoxia, facilitates the repolarization of pro-tumor M2 macrophages to antitumor M1 phenotypes, and attenuates immunosuppression within the TME. Moreover, localized copper accumulation efficiently induces cuproptosis, which synergizes with low-dose radiotherapy to enhance ICD. Accompanying DAMPs promote DCs maturation and activate robust antitumor immunity, ultimately establishing a novel copper-based low-dose radioimmunotherapy strategy (Figure 1).

Material and Methods

Materials

Black phosphorus nanosheets were obtained from XFNANO Materials Technology (China). Copper chloride dihydrate and tetrathiomolybdate were sourced from Aladdin (China). Glutathione and 5,5-dithiobis (2-nitrobenzoic acid) and methylene blue were supplied by Macklin (China). 4′,6-Diamidino-2-phenylindole, a reactive oxygen species assay kit and rabbit an-ti-DLAT antibody were purchased from Solarbio (China). A cell counting kit-8 (CCK-8) was sourced from Beyotime (China),

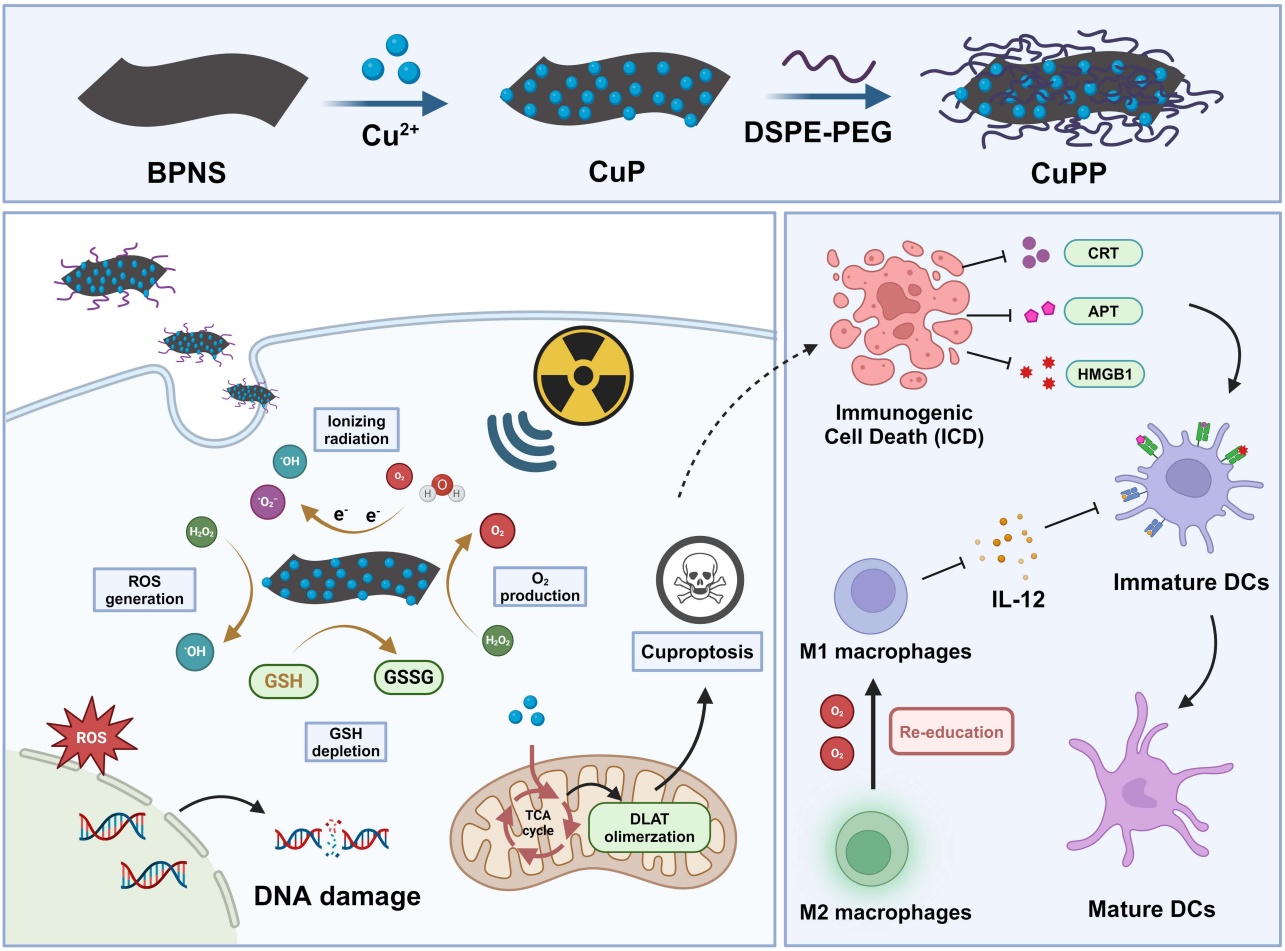

Figure 1 Schematic illustration of the BPNS@Cu-PEG nanoplatform and its proposed mechanism for cuproptosis-enhanced low-dose radioimmunotherapy. The diagram outlines the stepwise fabrication of BPNS@Cu-PEG and its multimodal mechanism of action, which combines radiosensitization, TME remodeling, and cuproptosis-induced immunogenic cell death to potentiate antitumor immunity under low-dose irradiation.

and 1,3-diphenylisobenzofuran was provided by MedChemExpress (USA). Calcein-AM/PI assay kits and Actin Tracker Red-594 dye were obtained from Beyotime (China). UK-5099 was purchased from Med-ChemExpress (USA). RPMI-1640 medium, Dulbecco's modified Eagle medium (DMEM), and fetal bovine serum (FBS) were obtained from Yeasen Biotechnology (China). IL-4 protein was sourced from Sino Biological (China), while anti-CD206-APC, anti-CD80-APC, and anti-CD86-PE antibodies were obtained from BioLegend (USA). Mouse IL-6, IL-10, IL-12, TNF-α, and HMGB1 ELISA kits were purchased from Neobioscience (China).

Cell Lines

4T1, DC2.4, NIH3T3, and RAW264.7 cells were obtained from Procell (China). All cells were cultured in a 5% CO_2 environment. For 4T1 and DC2.4 cells, RPMI-1640 medium containing 10% FBS was used for proliferation, while NIH3T3 and RAW264.7 cells were cultured in DMEM containing 10% FBS.

Synthesis of BPNS@Cu-PEG

A 500 μL reaction system was prepared containing 150 μL of BPNS dispersion (0.2 mg/mL), 250 μL of $CuCl_2$ solution (4 mM) and 100 μL of HEPES buffer (10 mM). The mixture was placed in a homogenizer and incubated for 3 h at 25 °C with agitation at 900 rpm. The BPNS@Cu nanoplatform was then obtained by centrifuging the mixture at 25 °C and 12,000 rpm for 20 min. The collected BPNS@Cu was redispersed in 250 μL of ultrapure water and combined with 250 μL of DSPE-PEG 2000 (2 mM). This mixed solution was ultrasonicated for 30 min in an ice bath, followed by

https://doi.org/10.2147/IJN.S563439

stirring for 24 h. The final solution was then centrifuged, washed twice with ultrapure water, and purified to yield BPNS@Cu-PEG. The prepared BPNS@Cu-PEG was stored at 4 °C for further use.

Characterization

Dynamic light scattering (DLS) and zeta potential measurements of BPNS, BPNS@Cu, and BPNS@Cu-PEG were conducted using a Zetasizer Pro (Malvern, UK). The surface morphology of BPNS@Cu-PEG was examined by transmission electron microscopy. The elemental composition of BPNS@Cu-PEG was analyzed via energy-dispersive X-ray spectroscopy (EDS). To assess stability, 0.5 mL samples of BPNS, BPNS@Cu, and BPNS@Cu-PEG (60 μg/mL) were placed in 1.5 mL centrifuge tubes and exposed to room temperature under natural environmental conditions. The absorbance of each sample was recorded at various time intervals using a microplate reader (SPARK, Switzerland).

GSH Depletion, ROS Generation, and O_2 Production

To assess GSH consumption by BPNS@Cu-PEG, 10 μL of GSH solution was added to varying concentrations of BPNS@Cu-PEG, then incubated at 37 °C for 10 min. Next, 10 μL of 5,5'-Dithio-bis-(2-nitrobenzoic acid)(DTNB) (10 mg/mL) was added to the mixture and incubated for 5 min, after which the absorbance of GSH in each group was recorded using a microplate reader. For •OH generation analysis, 100 μL of methylene blue (MB) solution (200 μg/mL) and 100 μL of 1 mM H_2O_2 were added to 800 μL of BPNS@Cu-PEG (0–50 μg/mL) and incubated at 37 °C for 10 min. The absorbance spectrum of MB was then analyzed to determine •OH production. To evaluate the generation of singlet oxygen ($^1O_2$), 1,3-Diphenylisobenzofuran (DPBF) solution was incubated with various concentrations of BPNS@Cu-PEG for 10 min, followed by exposure to X-rays (3 Gy). O_2 production induced by different concentrations of BPNS@Cu-PEG was measured using a portable dissolved oxygen detector. Electron spin resonance (ESR) technology was used in combination with specific spin trapping agents DMPO (5,5-dimethyl-1-pyrroline-N-oxide) and TEMP (2,2,6,6-tetramethylpiperidine) to capture •OH and $^1O_2$, respectively.

Cellular Uptake and Cytotoxicity

4T1 tumor cells were seeded into confocal dishes at a density of 8×10^4 cells and cultured for 12 h. Fresh medium containing Cy5-labeled BPNS@Cu-PEG (60 μg/mL) was then added and incubated with the cells for time points ranging from 0 to 6 h. Cellular internalization of BPNS@Cu-PEG was observed using laser confocal microscopy (LSM880, ZEISS, Germany). Additionally, single-cell suspensions were obtained by trypsinization, and flow cytometry was used to quantify Cy5 fluorescence levels in 4T1 cells following treatment with different concentrations of BPNS@Cu-PEG.

DC2.4, NIH3T3, RAW264.7 and 4T1 cells were seeded into 96-well plates at a density of 1×10^4 cells per well and cultured for 24 h. Following incubation, cells were treated with varying concentrations of BPNS@Cu-PEG (0–120 μg/mL) for 24 h. The CCK-8 assay was used to assess cell viability across different BPNS@Cu-PEG concentrations, both with and without X-ray irradiation. Additionally, the cytotoxicity of BPNS alone and the effects of different radiation doses were evaluated.

Cell Necrosis and Apoptosis

4T1 cells were seeded into 3.5 cm dishes at a density of 2×10^5 cells per dish and cultured for 12 h. Following treatment with BPNS, BPNS@Cu-PEG, or BPNS@Cu-PEG combined with X-ray irradiation, the live-to-necrotic cell ratio was assessed for the control, BPNS, BPNS@Cu-PEG, and BPNS@Cu-PEG+X groups using the Calcein-AM/PI detection kit. After a 12 h treatment with BPNS@Cu-PEG, 4T1 cells were irradiated with X-rays at a dose of 3 Gy for another 12 h. The live/necrotic cell ratio was then observed under a fluorescence microscope. For the analysis of tumor cells apoptosis at different stages, the cells were stained with Annexin V-FITC apoptosis assay kit after 6 h of different treatments and analyzed by flow cytometry.

Cellular ROS, GSH and O_2 Levels

4T1 cells were seeded into 3.5 cm dishes and subjected to different treatments: Control, BPNS, BPNS@Cu-PEG, and BPNS@Cu-PEG with X-ray irradiation. Following X-ray exposure, cells were cultured for an additional 4 h, then stained with 2',7'–Dichlorofluorescin Diacetate (DCFH-DA) for ROS analysis and ThiolTrace Violet 500 for GSH analysis. For O_2 detection, 4T1 cells were initially cultured in a hypoxic environment for 8 h, pretreated with $[Ru(dpp)_3]Cl_2$ (5 μM) for 3 h, and subsequently treated with BPNS or BPNS@Cu-PEG (60 μg/mL) for 8 h. The intracellular O_2 levels were then visualized using laser confocal microscopy.

JC-1 Staining and DNA Breakage Labeling

4T1 cells were seeded into 3.5 cm dishes at a density of 2×10^5 cells per dish and subjected to following treatments: Control, BPNS, BPNS@Cu-PEG, and BPNS@Cu-PEG with X-ray irradiation. After irradiation, the cells were incubated for an additional 4 h. Changes in mitochondrial membrane potential were assessed using JC-1 staining and visualized with a fluorescence microscope.

To evaluate tumor DNA damage, anti-γ-H2AX antibody was employed to assess DNA strand breakage across different treatment groups. Briefly, 4T1 cells were fixed with 4% paraformaldehyde and then incubated with 250 μL of γ-H2AX rabbit monoclonal antibody at 4 °C overnight. Following this, 250 μL of fluorescent secondary antibody was added and incubated at room temperature for 1 h. Cell nuclei were simultaneously stained with DAPI for 10 min, and the results were observed using laser confocal microscopy.

Cuproptosis and ICD

4T1 cells were seeded into confocal dishes and subjected to various treatment conditions. Following treatment, the cells were fixed and incubated with DLAT antibody, followed by a secondary antibody labeled with DyLight 488. Cell nuclei were stained with DAPI for 10 min, and all cell samples were imaged using laser confocal microscopy. Additionally, cuproptosis inhibitors (UK5099 and antimycin A) and Cu^{2+} chelators (tetrathiomolybdate and TTM) were employed for cuproptosis rescue experiments.

For ICD analysis, the seeded 4T1 cells were fixed in 4% paraformaldehyde and incubated with CRT antibody overnight. Subsequently, the cells were treated with a DyLight 488-labeled secondary antibody for 1 h, stained with DAPI for 10 min, and imaged using laser confocal microscopy. The supernatant from the treated 4T1 cells was collected for analysis of ATP levels and HMGB1 secretion using the corresponding ATP assay kit and HMGB1 ELISA kit.

Macrophage Polarization and DCs Maturation

RAW264.7 macrophages were first pretreated with 25 ng/mL interleukin-4 (IL-4) for 12 h to induce the generation of M2 macrophages. Following this, 4T1 cell supernatants treated with various factors were added to the macrophages and incubated for 24 h. The macrophage suspension was then collected and stained with CD86-PE and CD206-APC antibodies for 30 min. The fluorescence intensity was quantified using flow cytometry. Simultaneously, the supernatant from the macrophages was collected to analyze the secretion levels of the immune factors IL-10 and IL-12.

DC2.4 cells were seeded into 3.5 cm dishes at a density of 2×10^5 cells per dish and cultured for 12 h. The supernatant from 4T1 cells treated with various factors was then added and incubated with the DC2.4 cells for an additional 12 h. After incubation, the DC2.4 cell suspension was collected and stained with CD86-PE and CD80-APC antibodies for 30 min. The fluorescence intensity in the corresponding channels was quantified using flow cytometry. Additionally, the supernatant of the DC2.4 cells was collected, and the levels of immune factors (IL-6 and TNF-α) were measured using ELISA.

Animal Experiments

Female BALB/c mice (6–8 weeks old, 18–20 g) were obtained from Sijia Biotechnology Co., Ltd. The 4T1 tumor model was established by subcutaneous injection of 1×10^6 cells into the left lower limb. When tumors reached ~100 mm^3, mice were randomly divided into four groups (n = 8): saline control, X-ray irradiation alone (3 Gy × 3), BPNS@Cu-PEG

(4 mg/kg), and BPNS@Cu-PEG plus X-ray. Tumor volumes and body weights were monitored every 2 days using caliper measurements.

On day 8, three mice per group were sacrificed for sample collection. Lymph node single-cell suspensions were stained with anti-CD11c-FITC, anti-CD86-PE, and anti-CD80-APC antibodies to assess DCs maturation by flow cytometry. Tumor tissues were digested into single-cell suspensions for macrophage polarization analysis using anti-F4/80, anti-CD206, and anti-CD86 antibodies to distinguish M1 (F4/80+ CD86+) and M2 (F4/80+ CD206+) populations. Blood samples were collected and centrifuged to obtain plasma for immune factor and biochemical markers quantification. This comprehensive analysis enables the assessment of systemic immune responses and biosafety in the treatment groups.

Notably, for tumor cell inoculation, mice were anesthetized with 2% isoflurane in oxygen delivered by a precision nebulizer. For radiotherapy experiments, mice were anesthetized with an intraperitoneal injection of sodium pentobarbital (50 mg/kg). At the end of the experiment, all mice were euthanized by cervical dislocation under deep anesthesia with an overdose of pentobarbital sodium.

Statistical Analysis

All statistical analyses were conducted using one-way ANOVA in GraphPad Prism (v10.1), with quantitative results expressed as mean ± standard deviation (SD). Statistical significance was defined as a P value of less than 0.05. Significance levels are denoted as follows: ns (not significant); *$P < 0.05$; **$P < 0.01$; ***$P < 0.001$.

Results and Discussion

Synthesis and Characterization of BPNS@Cu-PEG

The synthesis process of BPNS@Cu-PEG was described in Figure 1. Briefly, copper ions were loaded onto the BPNS surface (BPNS@Cu) through metal-phosphorus coordination.[35] Then, DSPE-PEG 2000 was coated onto BPNS@Cu via ultrasonic blending to form BPNS@Cu-PEG nanoplatform. Changes in particle size and zeta potential confirmed the success of surface modification. As shown in Figure 2A, bare BPNS exhibited a hydrodynamic size of ~150 nm, which increased to ~200 nm after Cu^{2+} loading and to ~240 nm after PEG coating. The zeta potential indicated that bare BPNS carried a negative potential of -39.6 ± 1.5 mV, due to abundant phosphate anions on its surface. After Cu^{2+} modification, the potential shifted to -7.4 ± 2.5 mV, attributed to the coordination of Cu^{2+} with surface electrons on BPNS. After DSPE-PEG 2000 coating, the zeta potential increased further to -22.6 ± 2.1 mV (Figure 2B). Transmission electron microscopy (TEM) revealed BPNS@Cu-PEG nanoplatform with a size of 200 nm and a distinct coating layer (Figure 2C). Elemental composition analysis by using energy-dispersive X-ray spectroscopy (EDS) confirmed the presence of C, N, O, P, and Cu elements in BPNS@Cu-PEG (Figure 2D). These results demonstrate the successful synthesis of the BPNS@Cu-PEG nanoplatform. Additionally, inductively coupled plasma atomic emission spectrometry (ICP-AES) analysis showed that BPNS (60 μg/mL) coordinated with Cu^{2+} at a concentration of 1.86 ± 0.03 mM, meaning that approximately 93% of the added Cu^{2+} ions were successfully loaded, corresponding to about 1.98 μg of Cu^{2+} per 1 μg of BPNS (data not shown in figure).

BPNS is susceptible to oxidative degradation when exposed to H_2O and oxygen, which limits its broader application.[36,37] However, the stability of BPNS can be improved by coordinating its surface lone pair electrons with unsaturated metal ions. As shown in Figure S1A–C, BPNS, BPNS@Cu, and BPNS@Cu-PEG were stored under ambient conditions for 10 days. BPNS alone exhibited a substantial decrease in absorbance, with approximately 80% degradation over this period. In contrast, BPNS@Cu and BPNS@Cu-PEG displayed minimal absorbance changes, indicating that Cu^{2+} ion modification effectively enhanced BPNS stability. This increased stability is attributed to coordination interactions between BPNS surface electrons and Cu^{2+} ions, which effectively passivate active surface sites.[38] Furthermore, we monitored the size variation of BPNS@Cu-PEG under different pH conditions for 48 h. We observed rapid disintegration of the nanoparticles under acidic conditions (pH 4.8), demonstrating their high responsiveness to low-pH environments (Figure S2).

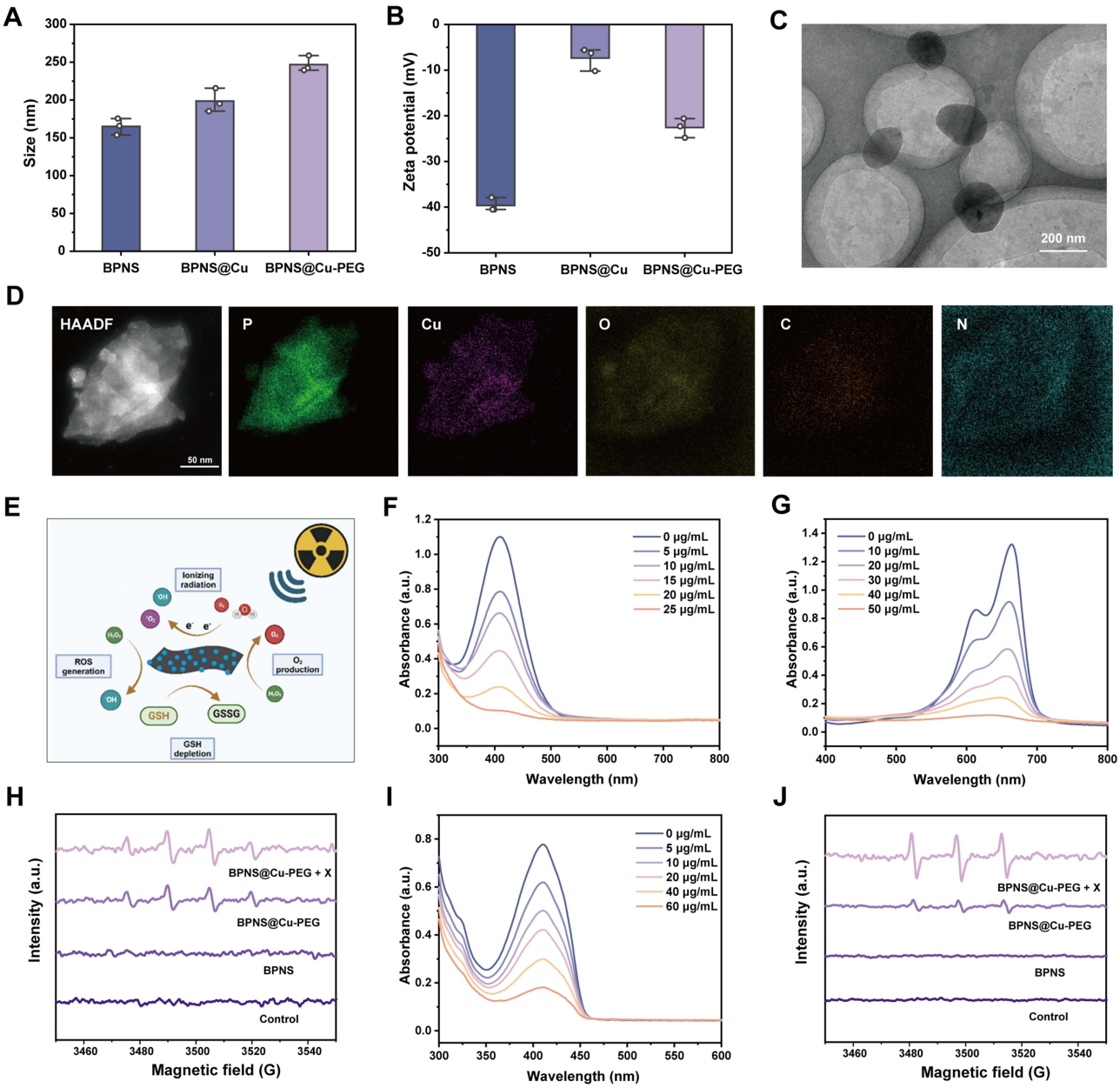

Figure 2 Characterization and reactive species generation of the BPNS@Cu-PEG nanoplatform. (**A**) Hydrodynamic size distribution of BPNS, BPNS@Cu, and BPNS@Cu-PEG (n = 3). Data are presented as mean ± s.d. (**B**) Zeta potential of BPNS, BPNS@Cu, and BPNS@Cu-PEG (n = 3). Data are presented as mean ± s.d. (**C**) Transmission electron microscopy (TEM) image of BPNS@Cu-PEG. Scale bar is 200 nm. (**D**) Elemental mapping of BPNS@Cu-PEG nanoplatform. Scale bar is 50 nm. (**E**) Schematic diagram of the BPNS@Cu-PEG nanoplatform-mediated the generation of •OH, $^1O_2$, and O_2. (**F**) Absorbance spectra of GSH after treatment with different concentrations of BPNS@Cu-PEG (0–25 μg/mL). (**G**) Absorbance spectra of MB after treatment with different concentrations of BPNS@Cu-PEG (0–50 μg/mL). (**H**) ESR spectroscopy of •OH generation in different treatment groups. (**I**) Absorbance spectra of DPBF after treatment with different concentrations of BPNS@Cu-PEG (0–60 μg/mL) under X-ray irradiation (3 Gy). (**J**) ESR spectroscopy of $^1O_2$ production in different treatment groups.

GSH Depletion, ROS Generation and O_2 Production

The presence of Cu^{2+} ion active centers in BPNS@Cu-PEG facilitates the continuous generation of O_2 and •OH, while consuming GSH, thereby alleviating tumor hypoxia and enhancing oxidative stress (Figure 2E). To explore the existence of active centers, we used the 5,5-dithiobis (2-nitrobenzoic acid) (DTNB), a specific probe that binds to GSH, forming a yellow chromogen, to evaluate the consumption of GSH induced by BPNS@Cu-PEG. As depicted in Figure 2F and Figure S3A, it was clearly observed that the rapid and continuous consumption of GSH when exposed to BPNS@Cu-PEG, as evidenced by gradual reduction in yellow color and a decrease in absorbance. Furthermore, we calculated the

https://doi.org/10.2147/IJN.S563439

GSH degradation efficiency at different BPNS@Cu-PEG concentrations, finding that only 25 μg/mL of BPNS@Cu-PEG could easily degrade ~90% of GSH withing 10 min (Figure S3B). During this process, Cu^{2+} ions could be reduced to Cu^{+}, which subsequently catalyze H_2O_2 to generate •OH via a Fenton-like reaction.[13] The generation of •OH induced by BPNS@Cu-PEG was quantified through methylene blue (MB) consumption. As shown in Figure 2G and Figure S4A, •OH production was concentration-dependent, with increasing BPNS@Cu-PEG concentrations leading to a significant decrease in MB absorbance and color fading. More than 50% of MB was rapidly degraded with only 20 μg/mL BPNS@Cu-PEG nanoplatform (Figure S4B).

To further verify the ability of the nanoplatform to induce the generation of •OH, we used ESR)spectroscopy for further analysis. As shown in Figure 2H, no obvious •OH signal was detected in the control group or BPNS group. However, a typical 1:2:2:1 quartet (attributed to DMPO-OH adduct) was observed in the BPNS@Cu-PEG group, indicating that the nanoplatform can effectively catalyze the generation of •OH. Notably, the characteristic signal intensity of •OH was significantly enhanced in the BPNS@Cu-PEG combined with X-ray irradiation group. This is mainly attributed to the synergistic catalytic effect induced by radiation, which converts H_2O into •OH.[39] In addition, considering that singlet oxygen ($^1O_2$) could also be generated during ionizing radiation,[40] we used 1,3-diphenylisobenzofuran (DPBF) to assess the $^1O_2$ generation by BPNS@Cu-PEG during radiation. As depicted in Figure 2I, the DPBF level decreased as BPNS@Cu-PEG concentration increased under X-ray irradiation (3 Gy), indicating enhanced $^1O_2$ production. In contrast, only a small amount of DPBF degradation occurred when exposed to X-ray irradiation alone, but significant DPBF consumption was observed when BPNS@Cu-PEG was combined with X-ray irradiation (Figure S5). The ESR spectroscopy was used to further verify the ability of the nanomaterial to induce the generation of $^1O_2$, with a triplet signal (Figure 2J). The radiosensitization of BPNS@Cu-PEG was explained by the ionization of electrons enriched on the surface of BPNS.[41] Additionally, Cu^{2+} present in BPNS@Cu-PEG can catalyze H_2O_2 into O_2 via catalase-like enzyme activity.[42] As shown in Figure S6, O_2 generation increased with BPNS@Cu-PEG in the presence of H_2O_2, suggesting that BPNS@Cu-PEG may help alleviate tumor hypoxia, thereby reducing radiation resistance.

Cellular Uptake and Toxicity

To investigate the cellular uptake of our prepared nanoplatform, BPNS@Cu-PEG was labeled with Cy5 to investigate the cellular uptake. Confocal laser scanning microscopy (CLSM) was used to observe the cellular endocytosis of the nanoplatform. As shown in Figure 3A, the Cy5 fluorescence signal (red) in the cells gradually increased over time, with the signal evenly distributed in the cytoplasm and no significant accumulation in the nucleus. In addition, flow cytometry analysis of Cy5 fluorescence further confirmed these findings. After 6 h of cellular uptake, the fluorescence value increased by about 10 times, indicating that BPNS@Cu-PEG nanoplatform could be effectively delivered into tumor cells. (Figure 3B and Figure S7).

To explore the cytotoxicity of the nanoplatform, different concentrations of BPNS@Cu-PEG (0–120 μg/mL) were co-incubated with normal cells (DC2.4, 3T3, and RAW264.7) and 4T1 breast tumor cells for 24 h. As shown in Figure 3C, the cytotoxicity of BPNS@Cu-PEG was concentration-dependent, with greater damage observed in tumor cells compared to normal cells. This increased sensitivity may be attributed to the elevated levels of H_2O_2 in the tumor microenvironment and pH responsiveness of BPNS@Cu-PEG, which enhances •OH generation by copper active centers in BPNS@Cu-PEG nanoplatform. In contrast, no significant cytotoxicity was observed, even at high concentrations of BPNS, indicating its good biocompatibility and safety (Figure S8A).

Furthermore, we evaluate the effect of BPNS@Cu-PEG in combination with X-ray irradiation on tumor cell viability. As shown in Figure S8B, we first examined the survival of tumor cells under varying radiation doses alone (0–8 Gy). The result showed that approximately 80% of 4T1 cells survived even at a radiation dose of up to 8 Gy. This suggests that single radiotherapy is likely to cause radiation resistance, leading to treatment failure treatment failure.[1,17] However, when BPNS@Cu-PEG (60 μg/mL) was combined with X-ray irradiation only at dose of 3 Gy, significant tumor cell necrosis was observed, as evidenced by the increase in red fluorescence (dead cells, labeled with PI) and the decrease in green fluorescence (live cells, labeled with Calcein-AM) (Figure 3D). The viability of 4T1 cells dropped to below 35% when BPNS@Cu-PEG was combined with low radiation dose (Figure 3E). In addition, we utilized Annexin V-FITC/PI staining to distinguish between early and late apoptotic cells. Early apoptotic cells were labeled solely by Annexin V-FITC, while late

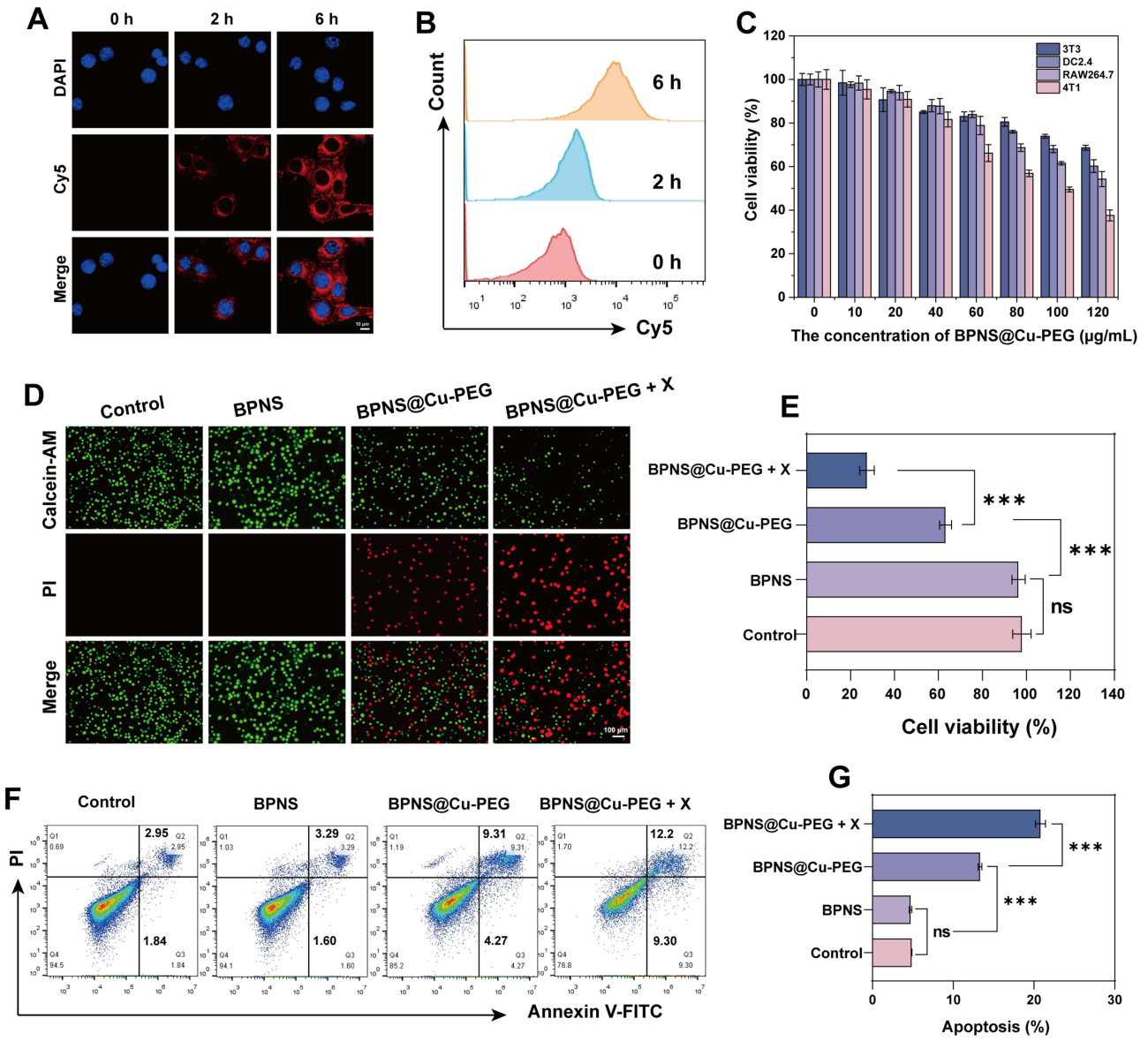

Figure 3 Cellular uptake, biocompatibility, and therapeutic efficacy of BPNS@Cu-PEG in vitro. (**A**) CLSM images of Cy5-labeled BPNS@Cu-PEG in 4T1 cells at various incubation times, where the cell nuclei were labeled by DPAI. Scale bar = 10 μm. (**B**) Flow cytometry quantitative analysis of the fluorescence intensity of 4T1 cells after incubation with BPNS for different time (n = 3). (**C**) Cytotoxicity evaluation of BPNS@Cu-PEG nanoplatform against 3T3, RAW264.7, DC2.4, and 4T1 cells at concentrations of 0–120 μg/mL (n = 3). (**D**) Fluorescence images of 4T1 cells after different treatments, assessed by Calcein-AM/PI double staining. Live cells with intact membranes are stained green by Calcein-AM, whereas dead cells with compromised membranes are stained red by PI. Scale bar = 100 μm. (**E**) Quantitative analysis of cell viability after different treatments, measured by the CCK-8 assay. (**F**) Analysis of early and late apoptosis in tumor cells after different treatments. (**G**) Flow cytometry analysis of tumor apoptotic cells (n = 3). All quantitative data are expressed as mean ± s.d. (n = 3 independent experiments). Statistical significance was calculated via by one-way analysis of variance (ANOVA). ***$P < 0.001$.

Abbreviation: ns, no significance.

apoptotic cells were labeled with both Annexin V-FITC and PI. As shown in Figure 3F and G, no significant difference in early and late apoptotic rates was observed between the BPNS and Control groups. However, when 4T1 cells were only treated with the nanoplatform for 6 h, the proportion of early apoptotic cells increased to 4.27% and the proportion of late apoptotic cells increased to 9.31%. When combined with 3 Gy of X-ray irradiation, these rates further increased to 9.30% for early apoptosis and 12.2% for late apoptosis. These results indicate that BPNS@Cu-PEG effectively induce apoptosis and necrosis in tumor cells, particularly when combined with low-dose radiotherapy.

https://doi.org/10.2147/IJN.S563439

TME Regulation by BPNS@Cu-PEG

The unique TME, characterized by elevated H_2O_2 and GSH levels as well as hypoxia, often leads to radioresistance and, consequently, to radiotherapy failure.[25] To investigate the BPNS@Cu-PEG-induced imbalance in redox homeostasis within tumors through the regulation of TME, we analyzed the levels of tumor endogenous ROS and GSH after different treatments. As shown in Figure 4A, weak fluorescence was observed in both the Control and BPNS groups, indicating minimal ROS generation. In contrast, significant green fluorescence was detected in BPNS@Cu-PEG group, confirming that the copper active center in BPNS@Cu-PEG could effectively catalyze ROS generation, mainly •OH. Notably, the strongest ROS fluorescence (including •OH and $^1O_2$) was observed when BPNS@Cu-PEG was combined with X-ray radiation at dose of 3 Gy, highlighting the sensitizing effect of BPNS@Cu-PEG on radiotherapy.

Considering the inherent antioxidant defense mechanism in tumor cells, characterized by abundant glutathione (GSH), which may lead to treatment failure,[24] we further analyzed the depletion of GSH caused by BPNS@Cu-PEG nanoplatform. As shown in Figure 4B, ThiolTrace Violet 500 was used to detect GSH level under different treatments. In contrast to ROS levels, the intracellular GSH content in the Control and BPNS groups remained high, as indicated by strong green fluorescence. However, after treating with BPNS@Cu-PEG, the intracellular GSH level significantly decreased, with further depletion observed when combined with X-ray treatment.

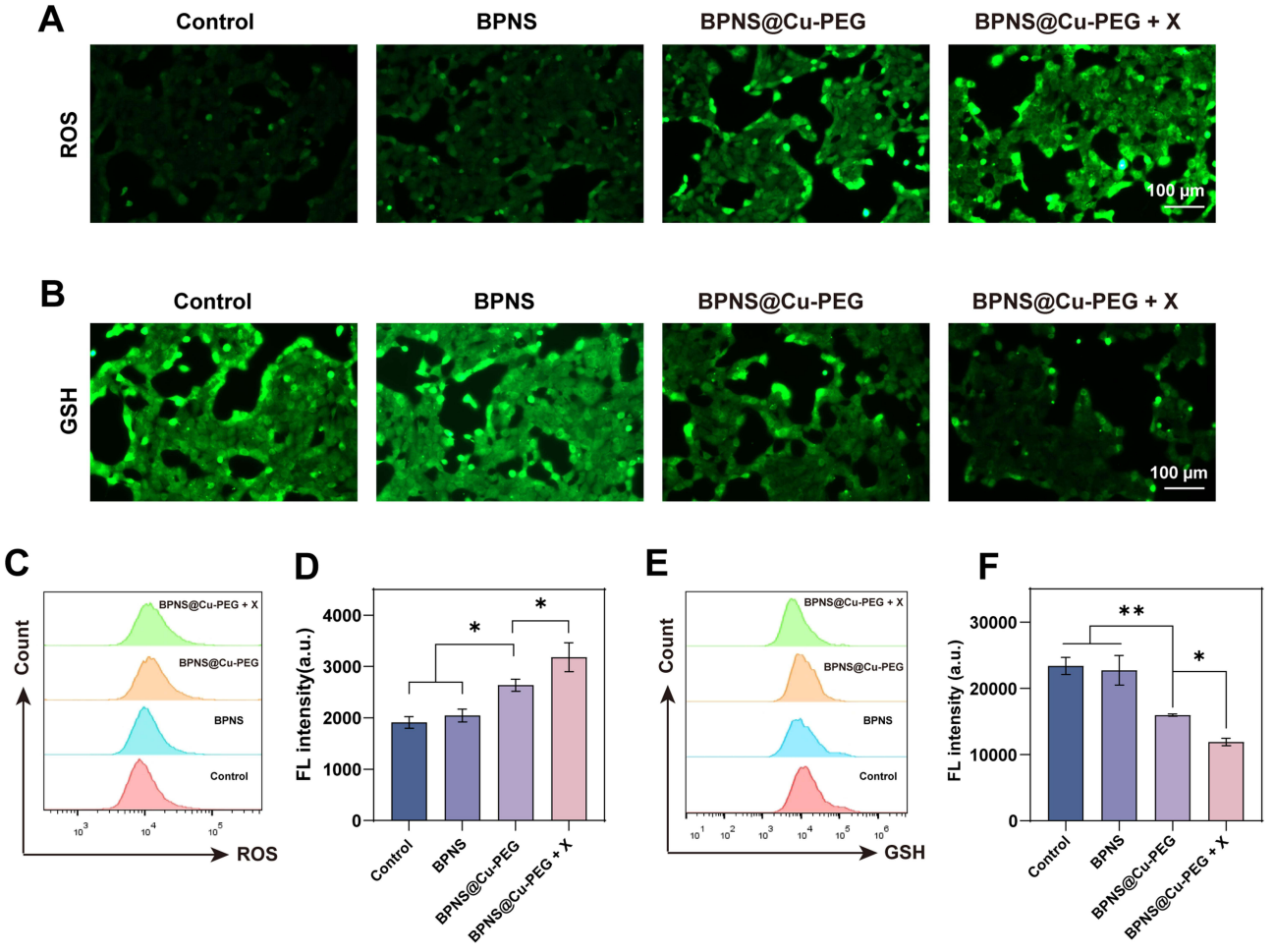

Figure 4 Modulation of ROS and GSH levels by BPNS@Cu-PEG. (**A**) Fluorescence images of ROS levels after different treatments as indicated. Scale bar = 100 μm. (**B**) Fluorescence images of GSH levels after different treatments. Scale bar = 100 μm. (**C**) Flow cytometry analysis of ROS in 4T1 cells following different treatments. (**D**) Flow cytometry for quantification of endogenous ROS levels in tumors (n = 3). (**E**) Flow cytometry analysis to assess endogenous GSH consumption under different conditions. (**F**) Flow cytometry analysis of GSH levels after different treatments (n = 3). Data are presented as mean ± s.d. from n = 3 biologically independent experiments. Statistical significance was calculated via by one-way analysis of variance (ANOVA). $^{**}P < 0.01$ and $^{*}P < 0.05$.

Moreover, we employed flow cytometry to quantify the ROS levels in 4T1 tumor cells. The results showed a slight increase in ROS after BPNS treatment, which may be related to cellular oxidative stress. However, BPNS@Cu-PEG significantly increased ROS levels due to the presence of copper active sites, and these levels were further increased in synergy with X-ray therapy ((Figure 4C and D)). Correspondingly, the depletion of GSH under these treatment conditions was further confirmed by flow cytometry (Figure 4E and F). These results indicate that the BPNS@Cu-PEG nanoplatform can effectively regulate the redox cycle in the tumor microenvironment.

Hypoxic tumor microenvironment is another important factor causing radioresistance.[43] Therefore, we measured O_2 generation following different treatments. $[Ru(dpp)_3]Cl_2$ is a ruthenium (II) complex that can be used to assess the oxygen level in the tumor microenvironment. As shown in Figure 5A. Strong red fluorescence was observed in both the Control group and the BPNS group, indicating that the cells were in a severe hypoxic environment. In contrast, after treatment with BPNS@Cu-PEG, it could be observed that the hypoxic signal was significantly weakened, which was consistent with cells under normoxic conditions. This is mainly attributed to the fact that BPNS@Cu-PEG could catalyze the conversion of intracellular H_2O_2 into O_2, effectively increase the intracellular O_2 level, and thus alleviate the hypoxic

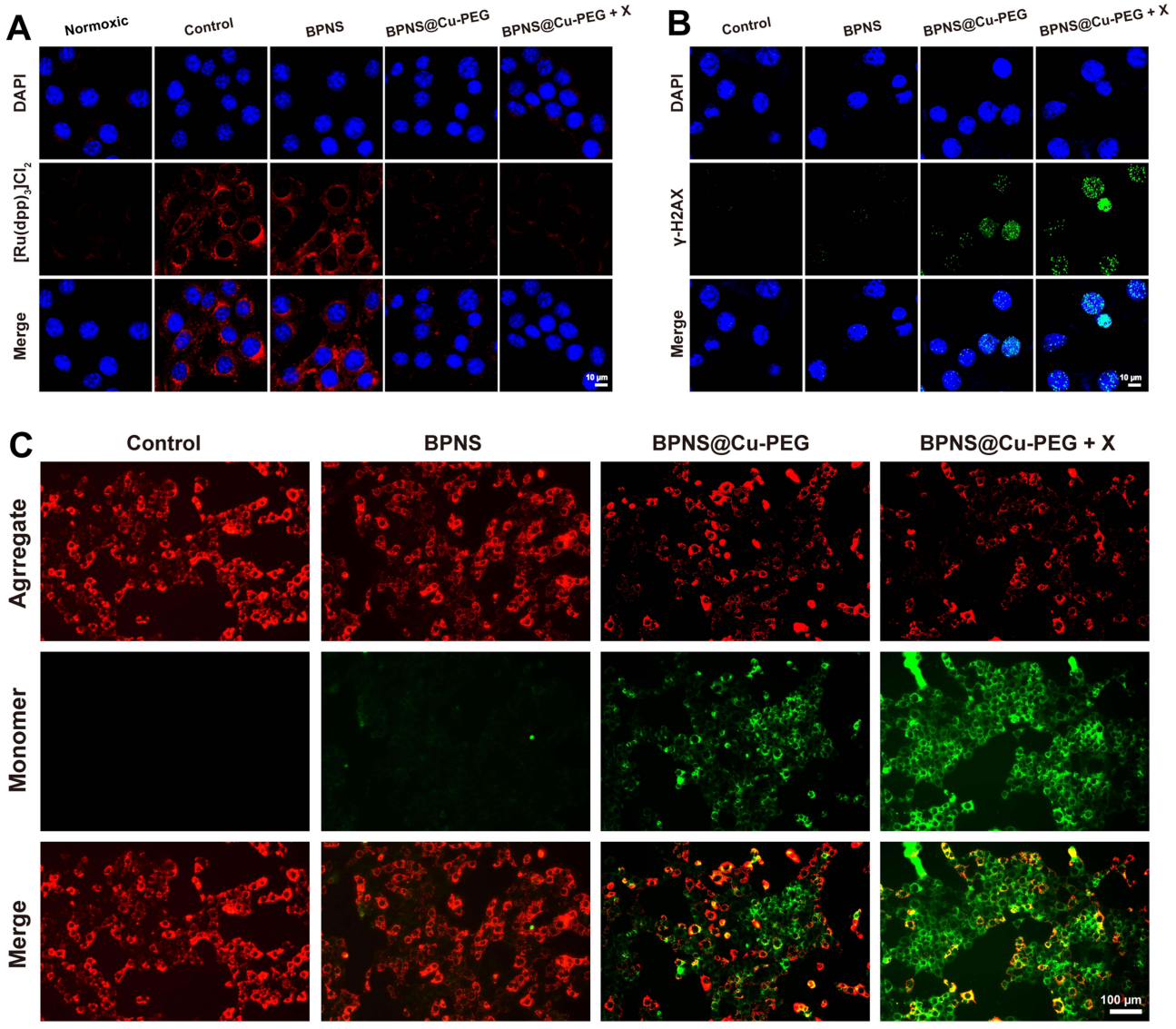

Figure 5 Oxygen generation, DNA damage, and mitochondrial impairment induced by BPNS@Cu-PEG. (**A**) CLSM images of intracellular O_2 production in 4T1 tumor cells following various treatments. Scale bar = 10 μm. (**B**) CLSM images of γ-H2AX levels (green fluorescence) after different treatments. Scale bar = 10 μm. (**C**) Fluorescent images illustrating mitochondrial damage after different treatments. Scale bar = 100 μm.

https://doi.org/10.2147/IJN.S563439

state. These results indicate that BPNS@Cu-PEG can actively consume endogenous GSH, promote the generation of ROS and O_2, regulate the hypoxic TME, and thus improve radiosensitivity.

Mitochondrial Damage and DNA Fragmentation

DNA double-strand breaks (DSBs) are considered one of the most severe forms of DNA damage. H2AX, a variant of the histone H2A, plays a critical role in the cellular response to DSBs. Upon the occurrence of double-strand breaks, H2AX is phosphorylated to form γ-H2AX, a well-established marker of DNA damage.[13,44] As shown in Figure 5B, a strong presence of γ-H2AX (green fluorescence marker) was observed after BPNS@Cu-PEG nanoplatform treatment, indicating significant DNA damage in tumor cells. Moreover, after combined X-ray exposure, the intensity of green fluorescence in the tumor cells was further enhanced, suggesting that radiosensitization contributed to aggravated DNA damage. In contrast, no significant DNA damage was detected in the Control and BPNS groups.

JC-1 is a widely used fluorescent probe for assessing mitochondrial membrane potential. Under normal conditions, JC-1 aggregates in the mitochondrial matrix to produce red fluorescence. However, when the mitochondrial membrane is compromised, JC-1 remains as a monomer and emits green fluorescence.[13,45] We employed JC-1 to evaluate mitochondrial membrane potential across different treatment groups. In the Control and BPNS groups, strong red fluorescence was evident, with negligible green fluorescence. However, the BPNS@Cu-PEG group exhibited notable green fluorescence, indicating that the mitochondrial membrane in tumor cells was ruptured. Following X-ray treatment, the intensity of green fluorescence increased significantly, demonstrating that the combination of BPNS@Cu-PEG and X-rays effectively induces mitochondrial membrane damage in tumor (Figure 5C). These findings highlight that the BPNS@Cu-PEG nanoplatform is capable of sensitizing radiotherapy, thereby achieving effective tumor damage even at low radiation doses.

Cuproptosis and ICD

Cuproptosis is a novel form of cell death that disrupts the TCA cycle through copper ions. It directly binds to DLAT, inducing DLAT oligomerization, leading to acute proteotoxic stress, mitochondrial metabolic depletion, and irreparable mitochondrial damage, ultimately causing tumor cell death.[23,27] To investigate the occurrence of cuproptosis induced by BPNS@Cu-PEG nanoplatform, we analyzed DLAT oligomerization in tumor cells under various exposure conditions. As expected in Figure 6A, no DLAT oligomerization signal was observed in the Control and BPNS groups, indicating the absence of DLAT oligomerization. In contrast, significant DLAT oligomers were detected in the BPNS@Cu-PEG group, accompanied by a clear green fluorescence signal, demonstrating cuproptosis induction by BPNS@Cu-PEG nanoplatform. Notably, after combined X-ray irradiation, a more pronounced aggregation of DLAT was observed. This enhancement may be due to radiation-induced damage to the mitochondrial membrane, which leads to easier accumulation of copper ions in mitochondria.[13,23]

To further elucidate that BPNS@Cu-PEG successfully mediates the occurrence of cuproptosis in tumor cells, we employed cuproptosis-related inhibitors and chelators, including copper apoptosis inhibitors (UK5099 and antimycin A) and copper chelators (tetrathiomolybdate, TTM). As shown in Figure 6B–D, we pre-treated 4T1 cells with these inhibitors and chelators. The results indicated that with increasing concentrations of inhibitors and chelators, the survival rate of 4T1 cells increased. Specifically, the viability of tumor cells rose to approximately 80%, 70%, and 70% after treatment with UK5099, antimycin A, and TTM, respectively. Among these, UK5099 demonstrated the most effective rescue, successfully restoring about 42% of the cells (Figure 6E). Furthermore, to investigate BPNS@Cu-PEG-mediated ICD under low-dose X-ray irradiation, we analyzed the release of DAMPs, including CRT translocation, HMGB1 and ATP secretion. As shown in Figure 6F, the CRT expression in tumor cells after treatment with BPNS@Cu-PEG significantly increased compared to the Control and BPNS groups, as evidenced by the strong fluorescence signal of CRT in the tumor cells. Notably, CRT expression further increased even with exposure to low doses of X-ray irradiation. The results for HMGB1 and ATP secretion paralleled the changes in CRT expression, emphasizing that the synergistic treatment of BPNS@Cu-PEG and X-ray effectively promotes tumor ICD (Figure 6G and H).

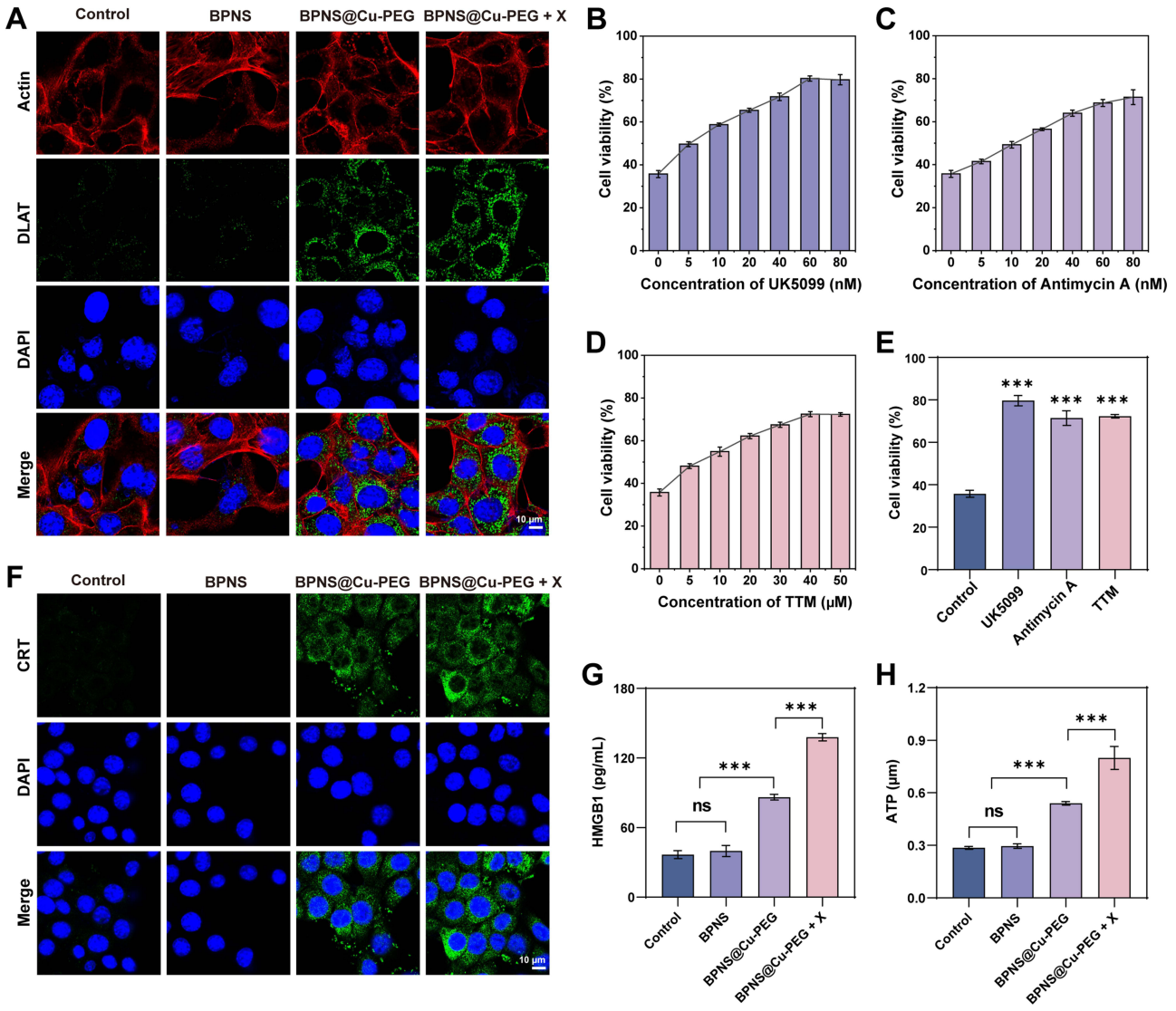

Figure 6 Cuproptosis induction, metabolic interference, and ICD marker expression. (**A**) Intracellular aggregation of DLAT proteins in tumor cells following various treatments where red fluorescence indicates Actin, green fluorescence indicates DLAT oligomers, and blue fluorescence represents DAPI. Scale bar = 10 μm. (**B**) Different concentrations of UK5099 interfered with BPNS@Cu-PEG-induced cytotoxicity (n = 3). (**C**) Different concentrations of Antimycin A interfered with BPNS@Cu-PEG-induced cytotoxicity (n = 3). (**D**) Different concentrations of TTM interfered with BPNS@Cu-PEG-induced cytotoxicity (n = 3). (**E**) Comparison of BPNS@Cu-PEG-induced cell viability after pretreatment with UK5099, antimycin A, and TTM at the highest concentration (n = 3). (**F**) Expression of CRT protein in 4T1 cells subjected to different treatments, with green fluorescence indicating CRT protein and blue fluorescence indicating DAPI. Scale bar = 10 μm. (**G**) Expression levels of HMGB1 protein in various treatment groups (n = 3). (**H**) ATP production in 4T1 cells after different treatments (n = 3). All quantitative data are presented as mean ± s.d.; n = 3 biologically independent experiments. Statistical significance was calculated via by one-way analysis of variance (ANOVA). ***$P < 0.001$.
Abbreviation: ns, no significance.

TAMs Repolarization and DCs Maturation

Encouraged by the effective activation of ICD by BPNS@Cu-PEG in vitro, we further explored its regulatory effects on the immunosuppressive TME, including the polarization of macrophages from the pro-tumoral M2 type to the anti-tumor M1 type, as well as the stimulation of DCs maturation. As shown in Figure 7A–D, compared with the control group, the M2 macrophages ($CD206^+$) decreased by about 45% after BPNS@Cu-PEG nanoplatform treatment. However, when it was combined with X-ray irradiation at dose of 3 Gy, the proportion of M2 macrophages was further reduced (~ 60%). Concurrently, the proportion of M1 macrophages marked by $CD86^+$ increased significantly in BPNS@Cu-PEG plus X-ray group, reaching approximately three times that of the Control group. This change is primarily attributed to the generation of ROS and O_2 mediated by BPNS@Cu-PEG, which efficiently promotes the repolarization of macrophages from the M2 to

https://doi.org/10.2147/IJN.S563439

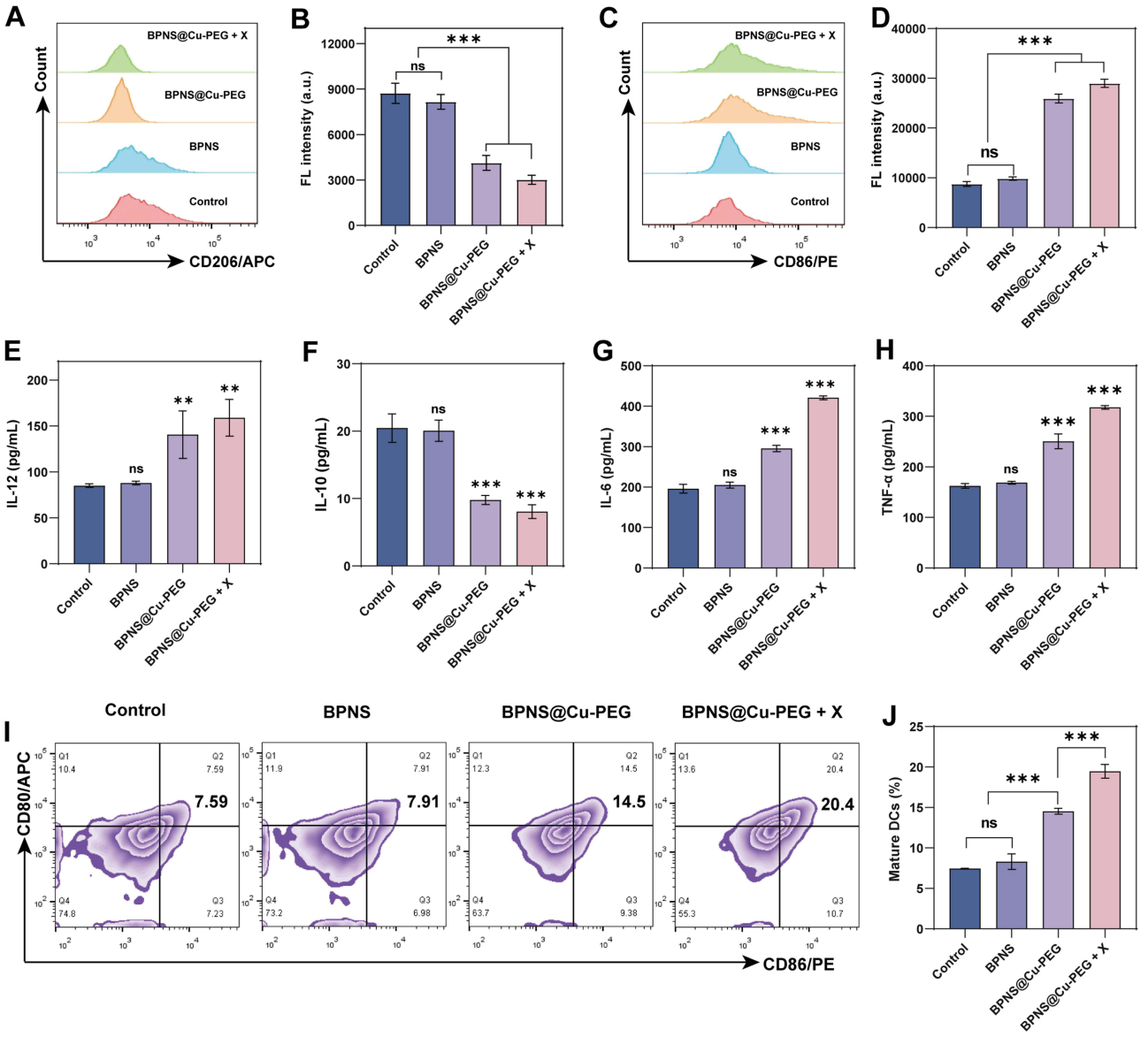

Figure 7 Polarization of M2 macrophages to M1 and maturation of DCs. (**A**) Representative flow cytometry plots of the proportion of M2 macrophages ($CD206^+$) after different treatments. (**B**) Fluorescence intensity of M2 macrophages after different treatments (n = 3). (**C**) Representative flow cytometry plots of the proportion of M1 macrophages ($CD86^+$) after different treatments. (**D**) Fluorescence intensity of M1 macrophages after different treatments (n = 3). (**E**) Analysis of IL-12 secretion levels in different treatment groups by ELISA (n = 3). (**F**) Analysis of IL-10 secretion levels in different treatment groups by ELISA (n = 3). (**G**) Detection of IL-6 secretion levels in different treatment groups (n = 3). (**H**) Analysis of TNF-α secretion after different treatments (n = 3). (**I**) Representative flow cytometry plots of DCs maturation ($CD86^+$, $CD80^+$) in vitro, following different treatments as indicated. (**J**) Analysis of the maturation ratio of DCs after different treatments (n = 3). All quantitative data are presented as mean ± s.d.; n = 3 biologically independent experiments. Statistical significance was calculated via by one-way analysis of variance (ANOVA). ***$P < 0.001$.
Abbreviation: ns, no significance.

the M1 phenotype.[10,26] Moreover, we assessed the levels of interleukin-12 (IL-12) and interleukin-10 (IL-10) using corresponding ELISA kits. The results, shown in Figure 7E and F, revealed that the IL-12 concentration increased by about 1.7 times compared with the control group, while the IL-10 concentration decreased to about half of the original level in the BPNS@Cu-PEG + X group. These findings further confirm the repolarization of TAMs from the M2 to the M1 phenotype induced by BPNS@Cu-PEG nanoplatform.

In addition, we used appropriate ELISA kits to detect the levels of pro-inflammatory factors secreted by immune cells, including interleukin-6 (IL-6) and tumor necrosis factor-α (TNF-α). As shown in Figure 7G and H, the expression levels of IL-6 and TNF-α were highest in the BPNS@Cu-PEG + X-ray combined treatment group. To further investigate immune activation, we quantified the proportion of mature DCs ($CD80^+$, $CD86^+$) following different treatments. As

illustrated in Figure 7I and J, the proportion of mature DCs in the BPNS@Cu-PEG group increased from the original 7.59% to 14.5%. Notably, the maturation of DCs further enhanced to 20.4% after treatment with BPNS@Cu-PEG in conjunction with X-ray irradiation. These results indicate that the combination of radiation and cuproptosis effectively activates ICD, thereby inducing an anti-tumor immune response.

In vivo Anti-Tumor Potency of BPNS@Cu-PEG

Encouraged by the excellent anti-tumor therapeutic effect of the BPNS@Cu-PEG nanoplatform in vitro, we further evaluated its performance in inducing cuproptosis and TME reprogramming, thereby enhancing tumor radioimmunotherapy in vivo. As shown in Figure 8A, we established a breast cancer tumor-bearing mouse model by subcutaneously inoculating 4T1 tumor cells. On day 7 post-inoculation, the mice were randomly divided into four groups (n = 8) and treated as follows: Control group (saline), X-ray irradiation group (3 Gy), BPNS@Cu-PEG group, and BPNS@Cu-PEG combined with X-ray irradiation group. The growth of tumor and body weight were monitored every two days. Compared with the Control group, the X-ray irradiation group showed a moderate tumor inhibition effect, with a tumor inhibition rate (TIR) of 11.33%. In contrast, intravenous injection of BPNS@Cu-PEG significantly enhanced tumor inhibition, suppressing 53.7% of tumor growth due to oxidative damage and cuproptosis. Notably, tumor growth was nearly completely inhibited in the combination group (BPNS@Cu-PEG + X-ray), as evidenced by the stable tumor growth curve, indicating that TME modulation and cuproptosis effectively potentiated radiotherapy (Figure S9).

Furthermore, we investigated the antitumor immune response induced by BPNS@Cu-PEG plus X-ray irradiation. As shown in Figure 8B and C, the X-ray irradiation group exhibited only a weak increase in the ratio of DCs maturation, from 15.0% to 17.7%, suggesting radiation therapy is easily limited by radioresistance and radiation dose. However, the BPNS@Cu-PEG + X-ray group showed a marked increase in mature DCs (36.8%), significantly higher than that in the X-ray-alone (17.7%) or BPNS@Cu-PEG-alone (23.3%) groups. This robust DCs maturation is critical for activating adaptive immunity and cross-priming effector T cells to initiate anti-tumor immune responses.

Given the immunosuppressive TME's role in radiotherapy resistance, we analyzed the infiltration of M2-type TAMs ($F4/80^+$ $CD206^+$) and M1-type TAMs ($F4/80^+$ $CD86^+$) in tumors. As shown in Figure 8D–G, BPNS@Cu-PEG treatment significantly reduced the proportion of M2-type macrophages (from 10.4% to 3.88%) and increased M1-type macrophages (from 6.26% to 9.39%), which was attributed to the hypoxia alleviation of TME. Moreover, combining BPNS@Cu-PEG with low-dose X-rays (3 Gy) further decreased M2-type macrophages to 2.37% and increased M1-type macrophages to 21.0%, attributed to oxidative stress accumulation in the tumor area.

To explore the occurrence of cuproptosis and ICD in vivo, The DLAT and HMGB1 protein levels in the tumor area were analyzed by ELISA kit. As shown in Figure 8H, DLAT levels increased significantly after BPNS@Cu-PEG treatment compared to the control and X-ray groups. Combined treatment further elevated DLAT levels, possibly due to radiation-induced oxidative stress. The occurrence of ICD is pivotal for radioimmunotherapy. As shown in Figure 8I, X-rays alone slightly increased HMGB1 levels, but were not sufficient to induce adequate immune responses, as evidenced by the weakly increased maturation ratio of DCs. In contrast, BPNS@Cu-PEG alone or in combination with X-rays significantly enhanced HMGB1 expression, indicating that BPNS@Cu-PEG has potent ICD-inducing and anti-tumor immunity, which may be due to the nanoplatform's weakened restriction on the immune tumor microenvironment. We further analyzed serum immune factor levels in tumor-bearing mice across treatment groups. As shown in Figure 8J and K, the combination of BPNS@Cu-PEG with X-ray irradiation elicited the highest expression of immune factor IL-6 and TNF-α, indicating the activation of potent innate and cellular immunity. To further verify the translatable antitumor immune effect, we investigated the level of IFN-γ. IFN-γ is a major secretory product of cytotoxic T cells, and its level reflects the induction of systemic adaptive immune responses. As shown in Figure S10, compared with the control group and the X-ray group, IFN-γ secretion was significantly increased after BPNS@Cu-PEG treatment, and the combined treatment with low-dose radiotherapy further increased IFN-γ secretion levels. These results collectively indicate that copper apoptosis sensitization and TME remodeling synergistically enhance the efficacy of radioimmunotherapy, and overcame the dose-dependent limitations of conventional radiotherapy.

In addition, we also analyzed the biosafety of BPNS@Cu-PEG combined with low-dose radiotherapy. As shown in Figure S11, there was no significant change in the weight of mice in different treatment groups, indicating minimal

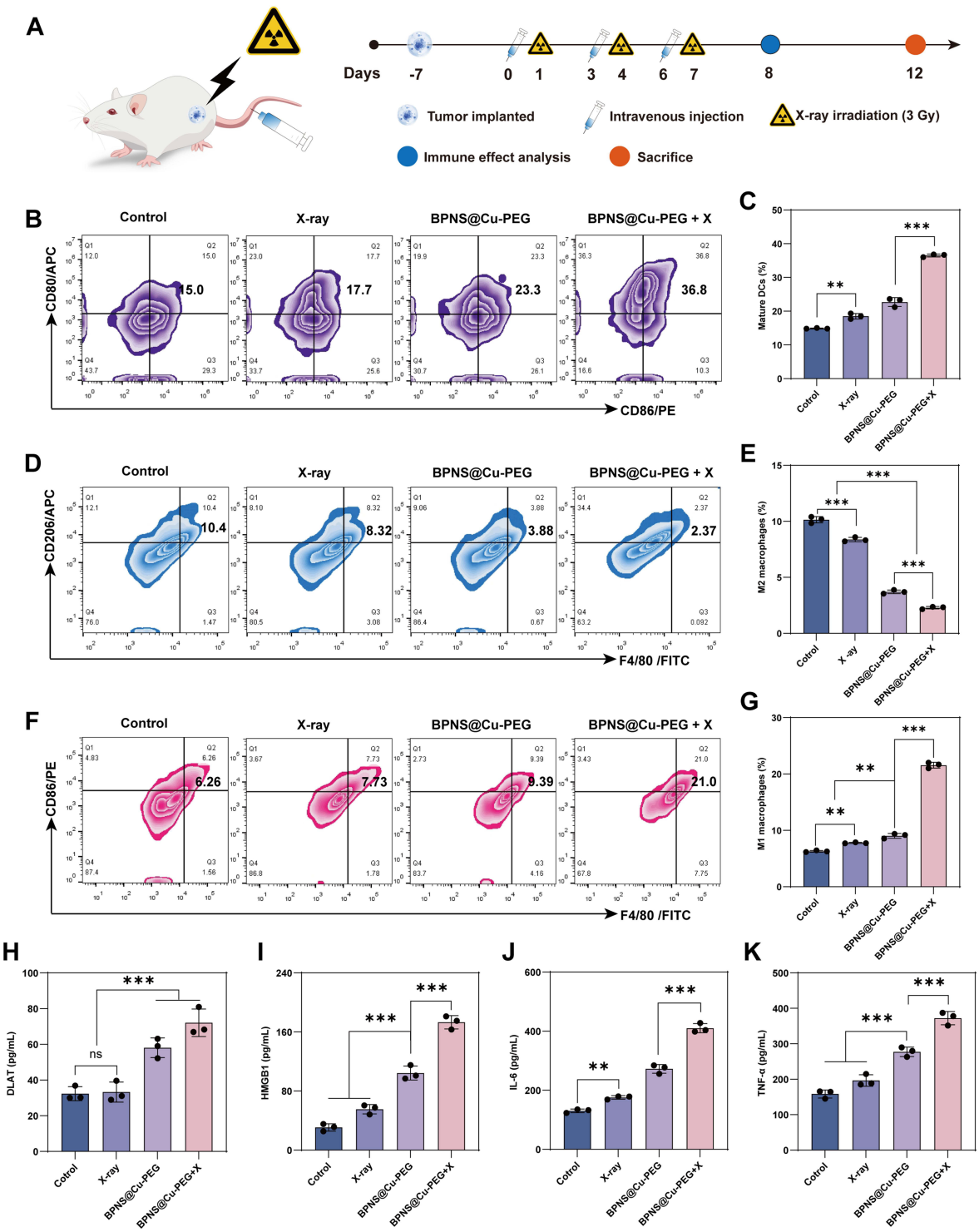

Figure 8 In vivo evaluation of BPNS@Cu-PEG combined with low-dose radiation strategy. (**A**) Experimental timeline and treatment scheme for the 4T1 tumor-bearing mouse model. (**B**) Representative flow cytometric analysis of mature DCs ($CD11c^+$ $CD80^+$ $CD86^+$) in lymph nodes after different treatments. (**C**) Quantitative analysis of DCs maturation rates across treatment groups. Data represent mean values ± SD (n = 3). (**D**) Representative flow cytometry plots of M2-type macrophages ($F4/80^+$ $CD206^+$) in tumor site. (**E**) Quantification of M2 macrophage infiltration in tumors. Data represent mean values ± SD (n = 3). (**F**) Representative flow cytometry plots of M1-type macrophages ($F4/80^+$ $CD86^+$) in tumor area. (**G**) Percentage of M1 macrophages in tumor tissues. Data represent mean values ± SD (n = 3). (**H, I**) DLAT levels (**H**) and HMGB1 level (**I**) in tumor lysates after different treatments. Data represent mean values ± SD (n = 3). (**J, K**) Serum cytokine levels of IL-6 (**J**) and TNF-α (**K**) post-treatment. Data represent mean values ± SD (n = 3). All quantitative data are presented as mean ± s.d.; n = 3 biologically independent experiments. Statistical significance was calculated via by one-way analysis of variance (ANOVA). $^{**}P < 0.01$; $^{***}P < 0.001$.

Abbreviation: ns, no significance.

toxicity of BPNS@Cu-PEG. Hemolysis assays further confirmed the nanoplatforms biocompatibility with less than 2% hemolysis even BPNS@Cu-PEG up to 250 μg/mL (Figure S12). In addition, no organ damage or obvious pathological changes were observed in major organs (heart, liver, spleen, lung, and kidney) (Figure S13). At the same time, we analyzed the blood biochemical indicators of different treatment groups to reflect their organ toxicity. Blood urea nitrogen (BUN) and creatinine (CREA) are key indicators for evaluating kidney function, and alanine aminotransferase (ALT) and aspartate aminotransferase (AST) are used for indicators of liver cell damage or necrosis. As shown in Figure S14A–D, no obvious abnormality of indicators was observed in the no-treatment group, indicating that the BPNS@Cu-PEG combined with low-dose radiation strategy has a high therapeutic safety.

Conclusion

In summary, we have developed a high-copper-loaded black phosphorus nanosheet platform (BPNS@Cu-PEG), engineered to pioneer a novel and synergistic paradigm for low-dose radioimmunotherapy. This work distinguishes itself from previous studies by establishing a fully integrated and self-reinforcing therapeutic cascade, which concurrently orchestrates TME remodeling, potent cuproptosis induction, and enhanced radiosensitization within a single, biodegradable nanoplatform.

The core innovation of our strategy lies in the unique multi-functionality of the BPNS@Cu-PEG nanoplatform. It acts as a master regulator of the TME by depleting the antioxidant GSH and catalyzing the generation of ROS, thereby inducing lethal oxidative stress. Simultaneously, the sustained production of oxygen not only alleviates tumor hypoxia to reduce radioresistance but also serves as a critical signal to repolarize immunosuppressive M2 macrophages to tumoricidal M1 phenotypes, effectively reversing one of the major barriers to immunotherapy. Furthermore, the efficient intracellular release of copper ions directly targets mitochondrial metabolism, triggering cuproptosis through toxic protein aggregation and irreversible mitochondrial dysfunction.

A key differentiating feature of our platform is the central role of biodegradable black phosphorus. Unlike many non-degradable or less efficient metal-based carriers, BPNS serves a dual role: it is both a high-capacity reservoir for copper via stable coordination bonds and an intrinsically potent radiosensitizer. This dual functionality ensures that the platform not only enhances localized X-ray energy deposition for low-dose radiotherapy but also does so in a biocompatible manner, degrading into harmless phosphates. This precise synergy between cuproptosis and the enhanced radiotherapy potently stimulates a robust ICD, leading to the exposure and release of DAMPs. The culmination of this coordinated attack is the potent activation of systemic anti-tumor immunity.

Overall, this study establishes a groundbreaking and distinctive nanoplatform that effectively bridges potent cuproptosis induction with low-dose radiotherapy. The integrated design, which couples comprehensive TME remodeling with a self-amplifying therapeutic cycle, demonstrates significant promise as a cascade anti-tumor strategy. We anticipate that the BPNS@Cu-PEG platform will open new avenues for the development of safe and highly effective radioimmunotherapy, presenting a compelling and translatable approach with considerable potential for future clinical application.

Ethical Statement

All animal experiments were approved by the Animal Ethics Committee of Jinan Maternal and Child Health Hospital (Approval No: KYW-25-002). The laboratory animal welfare adheres to Guidelines for Welfare and Ethical Review of Laboratory Animals (GB/T 35892-2018).

Funding

This work was supported by the Creative Youth Science Fund Project of Fujian Provincial Natural Science Foundation of China (Grant No. 2025J08049 and No. 2025J08041) and Medical and Health Science and Technology Project (Grant No. 202305020433).

Disclosure

The authors report no conflicts of interest in this work.

References

1. Bodei L, Herrmann K, Schöder H, Scott AM, Lewis JS. Radiotheranostics in oncology: current challenges and emerging opportunities. *Nat Rev Clin Oncol*. 2022;19(8):534–550. doi:10.1038/s41571-022-00652-y
2. Zhang Z, Liu X, Chen D, Yu J. Radiotherapy combined with immunotherapy: the Dawn of cancer treatment. *Sig Transduct Target Ther*. 2022;7(1):258. doi:10.1038/s41392-022-01102-y
3. Grassberger C, Ellsworth SG, Wilks MQ, Keane FK, Loeffler JS. Assessing the interactions between radiotherapy and antitumour immunity. *Nat Rev Clin Oncol*. 2019;16(12):729–745. doi:10.1038/s41571-019-0238-9
4. Galluzzi L, Guilbaud E, Schmidt D, Kroemer G, Marincola FM. Targeting immunogenic cell stress and death for cancer therapy. *Nat Rev Drug Discov*. 2024;23(6):445–460. doi:10.1038/s41573-024-00920-9
5. Wang P, Zhao X, Ying Y, et al. Programmed Nanosystem for Synergistic Immunogenic Cell Death Enhancing Radiotherapy-Mediated Abscopal Effect. *Adv Funct Mater*. 2025;35(2):2412497. doi:10.1002/adfm.202412497
6. Galassi C, Klapp V, Yamazaki T, Galluzzi L. Molecular determinants of immunogenic cell death elicited by radiation therapy. *Immunol Rev*. 2024;321(1):20–32. doi:10.1111/imr.13271
7. Chen M, Chen L, Mao K, et al. Therapeutic application of nanosystems-based metalloptosis for enhanced tumor radiotherapy. *Coord Chem Rev*. 2025;536:216666. doi:10.1016/j.ccr.2025.216666
8. Xu L, Peng M, Gao T, et al. Nanoenabled Intracellular Metal Ion Homeostasis Regulation for Tumor Therapy. *Adv Sci*. 2024;11(7):2306203. doi:10.1002/advs.202306203
9. Wei M, Bai J, Shen X, et al. Glutathione-Exhausting Nanoprobes for NIR-II Fluorescence Imaging-Guided Surgery and Boosting Radiation Therapy Efficacy via Ferroptosis in Breast Cancer. *ACS Nano*. 2023;17(12):11345–11361. doi:10.1021/acsnano.3c00350
10. Jiang X, Wu D, Xie W, Liu X, Zheng J. A pH-Sensitive Nanoparticle as Reactive Oxygen Species Amplifier to Regulate Tumor Microenvironment and Potentiate Tumor Radiotherapy. *IJN*. 2024;19:709–725. doi:10.2147/IJN.S436160
11. Xu M, Xu C, Qiu Y, et al. Zinc-based radioenhancers to activate tumor radioimmunotherapy by PD-L1 and cGAS-STING pathway. *J Nanobiotechnol*. 2024;22(1):782. doi:10.1186/s12951-024-02999-z
12. Chen R, Gong J, Yu Z, et al. X-ray triggered bimetallic nanoassemblies as radiosensitizers and STING agonists for a CDT/radio-immunotherapy strategy. *Acta Biomater*. 2025;192:366–376. doi:10.1016/j.actbio.2024.12.030
13. Jiang X, Wang J, Huang W, et al. Tumor Microenvironment Reprogrammed Bimetallic Hybrid Nanostimulator for Triggering Radio-Cuproptosis-Immunotherapy. *Adv Healthcare Materials*. 2024;13(30):2401902. doi:10.1002/adhm.202401902
14. Xiong Y, Li J, Jiang X, Zhen W, Ma X, Lin W. Nitric Oxide-Releasing Nanoscale Metal-Organic Layer Overcomes Hypoxia and Reactive Oxygen Species Diffusion Barriers to Enhance Cancer Radiotherapy. *Adv Sci*. 2025;12(8):2413518. doi:10.1002/advs.202413518
15. Li R, Zhao W, Han Z, et al. Self-Cascade Nanozyme Reactor as a Cuproptosis Inducer Synergistic Inhibition of Cellular Respiration Boosting Radioimmunotherapy. *Small*. 2024;20(25):2306263. doi:10.1002/smll.202306263
16. Liu J, Hu F, Wu M, et al. Bioorthogonal Coordination Polymer Nanoparticles with Aggregation-Induced Emission for Deep Tumor-Penetrating Radio- and Radiodynamic Therapy. *Adv Mater*. 2021;33(9):2007888. doi:10.1002/adma.202007888
17. Jiang R, Fang Q, Liu W, Chen L, Yang H. Recent Progress in Radiosensitive Nanomaterials for Radiotherapy-Triggered Drug Release. *ACS Appl Mater Interfaces*. 2025;17(10):14801–14821. doi:10.1021/acsami.4c23023
18. Wang S, Cheng M, Wang S, et al. A Self-Catalytic NO/O_2 Gas-Releasing Nanozyme for Radiotherapy Sensitization through Vascular Normalization and Hypoxia Relief. *Adv Mater*. 2024;2024:2403921. doi:10.1002/adma.202403921
19. Harris MA, Savas P, Virassamy B, et al. Towards targeting the breast cancer immune microenvironment. *Nat Rev Cancer*. 2024;24(8):554–577. doi:10.1038/s41568-024-00714-6
20. Huang Z, Huang S, Song S, et al. Two-dimensional coordination risedronate-manganese nanobelts as adjuvant for cancer radiotherapy and immunotherapy. *Nat Commun*. 2024;15(1):8692. doi:10.1038/s41467-024-53084-w
21. Kahlson MA, Dixon SJ. Copper-induced cell death. *Science*. 2022;375(6586):1231–1232. doi:10.1126/science.abo3959
22. Huang J, Hu F, Zhang H, et al. Ultrasound-Triggered Nanoparticles Induce Cuproptosis for Enhancing Immunogenic Sonodynamic Therapy. *Adv Mater*. 2025;2025:2504228. doi:10.1002/adma.202504228
23. Liao Y, Wang D, Gu C, et al. A cuproptosis nanocapsule for cancer radiotherapy. *Nat Nanotechnol*. 2024;19(12):1892–1902. doi:10.1038/s41565-024-01784-1
24. Lu S, Li Y, Yu Y. Glutathione-Scavenging Celastrol-Cu Nanoparticles Induce Self-Amplified Cuproptosis for Augmented Cancer Immunotherapy. *Adv Mater*. 2024;36(35):2404971. doi:10.1002/adma.202404971
25. Zhao P, Wang H, Zhao H, et al. Tumor microenvironment-reprogrammable CpG-templated copper sulfide loaded with disulfiram for sensitized cuproptosis immunotherapy. *Chem Eng J*. 2024;487:150524. doi:10.1016/j.cej.2024.150524
26. Pei P, Wang Y, Shen W, et al. Oxygen-driven cuproptosis synergizes with radiotherapy to potentiate tumor immunotherapy. *Aggregate*. 2024;5(3):e484. doi:10.1002/agt2.484
27. Chan L, Liu Y, Chen M, et al. Cuproptosis-Driven Enhancement of Thermotherapy by Sequentially Response Cu_{2-x} Se via Copper Chemical Transition. *Adv Funct Mater*. 2023;33(33):2302054. doi:10.1002/adfm.202302054
28. Luo H, Cao H, Jia H, et al. EISA in Tandem with ICD to Form In Situ Nanofiber Vaccine for Enhanced Tumor Radioimmunotherapy. *Adv Healthcare Materials*. 2023;12(27):2301083. doi:10.1002/adhm.202301083
29. He M, Zhang M, Xu T, et al. Enhancing photodynamic immunotherapy by reprograming the immunosuppressive tumor microenvironment with hypoxia relief. *J Control Release*. 2024;368:233–250. doi:10.1016/j.jconrel.2024.02.030
30. Liu W, Dong A, Wang B, Zhang H. Current Advances in Black Phosphorus-Based Drug Delivery Systems for Cancer Therapy. *Adv Sci*. 2021;8(5):2003033. doi:10.1002/advs.202003033
31. Qiu M, Singh A, Wang D, et al. Biocompatible and biodegradable inorganic nanostructures for nanomedicine: silicon and black phosphorus. *Nano Today*. 2019;25:135–155. doi:10.1016/j.nantod.2019.02.012
32. Qin L, Jiang S, He H, Ling G, Zhang P. Functional black phosphorus nanosheets for cancer therapy. *J Control Release*. 2020;318:50–66. doi:10.1016/j.jconrel.2019.12.013

33. Fu H, Feng L, Liang Q, Xiao X. Defect-Rich BiO_{2-x} -BP Composite Nanoplatform: a Synergistic Approach for X-Ray and Near-Infrared-Enhanced Cancer Radiodynamic Therapy. *Adv Healthcare Materials*. 2025;14(10):2404815. doi:10.1002/adhm.202404815
34. Cui X, Tang X, Niu Y, et al. Functional phosphorene: burgeoning generation, two-dimensional nanotherapeutic platform for oncotherapy. *Coord Chem Rev*. 2024;507:215744. doi:10.1016/j.ccr.2024.215744
35. Liu Y, Wang Y, Song S, Zhang H. Tumor Diagnosis and Therapy Mediated by Metal Phosphorus-Based Nanomaterials. *Adv Mater*. 2021;33 (49):2103936. doi:10.1002/adma.202103936
36. Liu Y, Gao P, Zhang T, et al. Azide Passivation of Black Phosphorus Nanosheets: covalent Functionalization Affords Ambient Stability Enhancement. *Angew Chem Int Ed*. 2019;58(5):1479–1483. doi:10.1002/anie.201813218
37. Xie C, Wang L, Liu Y, et al. Fullerene Covalent Passivation of Black Phosphorus Nanosheets toward Enhanced Near-Infrared-II Photothermal Therapy. *ACS Appl Mater Interfaces*. 2023;15(17):20686–20696. doi:10.1021/acsami.3c01074
38. Hu K, Xie L, Zhang Y, et al. Marriage of black phosphorus and Cu2+ as effective photothermal agents for PET-guided combination cancer therapy. *Nat Commun*. 2020;11(1):2778. doi:10.1038/s41467-020-16513-0
39. Lv B, Zhang H, Zheng X, et al. Structure-oriented catalytic radiosensitization for cancer radiotherapy. *Nano Today*. 2020;35:100988. doi:10.1016/j.nantod.2020.100988
40. Carulli F, He M, Cova F, Erroi A, Li L, Brovelli S. Silica-Encapsulated Perovskite Nanocrystals for X-ray-Activated Singlet Oxygen Production and Radiotherapy Application. *ACS Energy Lett*. 2023;8(4):1795–1802. doi:10.1021/acsenergylett.3c00234
41. Chan L, Chen X, Gao P, et al. Coordination-Driven Enhancement of Radiosensitization by Black Phosphorus *via* Regulating Tumor Metabolism. *ACS Nano*. 2021;15(2):3047–3060. doi:10.1021/acsnano.0c09454
42. Liu J, Zhu Y, Fan Y, et al. The pH-dependent multiple nanozyme activities of copper-cerium dioxide and its application in regulating intracellular oxygen and hydrogen peroxide levels. *J Colloid Interface Sci*. 2024;654:1054–1062. doi:10.1016/j.jcis.2023.10.050
43. Qiao Y, Yang F, Xie T, et al. Engineered algae: a novel oxygen-generating system for effective treatment of hypoxic cancer. *Sci Adv*. 2020;6(21): eaba5996. doi:10.1126/sciadv.aba5996
44. Chen B, Xiao L, Wang W, et al. $Bi_{2-x}Mn_xO_3$ Nanospheres Engaged Radiotherapy with Amplifying DNA Damage. *ACS Appl Mater Interfaces*. 2023;15(28):33903–33915. doi:10.1021/acsami.3c06838
45. Yao X, Yang H, Guo S, et al. Radiation-triggerable bioreactors enable bioenergetic reprograming of cancer stem cell plasticity via targeted arginine metabolism disruption for augmented radio-immunotherapy. *Biomaterials*. 2025;322:123391. doi:10.1016/j.biomaterials.2025.123391